2ⁿᵈ Advanced Optical Metrology Compendium

Facile Electron Transfer in Atomically Coupled Heterointerface for Accelerated Oxygen Evolution

Kassa Belay Ibrahim,* Tofik Ahmed Shifa, Paolo Moras, Elisa Moretti, and Alberto Vomiero*

An efficient and cost-effective approach for the development of advanced catalysts has been regarded as a sustainable way for green energy utilization. The general guideline to design active and efficient catalysts for oxygen evolution reaction (OER) is to achieve high intrinsic activity and the exposure of more density of the interfacial active sites. The heterointerface is one of the most attractive ways that plays a key role in electrochemical water oxidation. Herein, atomically cluster-based heterointerface catalysts with strong metal support interaction (SMSI) between WMn_2O_4 and TiO_2 are designed. In this case, the WMn_2O_4 nanoflakes are uniformly decorated by TiO_2 particles to create electronic effect on WMn_2O_4 nanoflakes as confirmed by X-ray absorption near edge fine structure. As a result, the engineered heterointerface requires an OER onset overpotential as low as 200 mV versus reversible hydrogen electrode, which is stable for up to 30 h of test. The outstanding performance and long-term durability are due to SMSI, the exposure of interfacial active sites, and accelerated reaction kinetics. To confirm the synergistic interaction between WMn_2O_4 and TiO_2, and the modification of the electronic structure, high-resolution transmission electron microscopy (HR-TEM), X-ray photoemission spectroscopy (XPS), and X-ray absorption spectroscopy (XAS) are used.

1. Introduction

Oxygen electrochemistry plays a major role in energy conversion and storage devices, particularly in the field of fuel cells, metal-air batteries, and water electrolyzers.[1] However, this technology has many particular bottlenecks. The major challenge in metal-air batteries and water electrolysis is to architect an economically feasible, earth-abundant, inexpensive, efficient electrocatalyst for the oxygen evolution reaction (OER).[2] Therefore, developing effective electrocatalyst for OER is critical in advancing these electrochemical devices toward commercialization.[3]

Frequently, an assortment of micro-/nano-structured simple metal oxides such as iron oxide,[4] manganese oxide, and cobalt oxide have drawn much consideration as the ideal catalysts in water oxidation. However, the well-known limited conductivity of metal oxides affects the use of these catalysts in water splitting. Owing to the promising activity of MnO_x in OER,[5] partial doping of MnO_x with W to form spinel oxide may offer a synergistic effect originating from the intrinsic characteristics of these two metal elements. Spinel oxides (represented with AB_2O_4 where A and B are metal ions)[6] are regarded as potential candidates in replacing precious metals due to their outstanding catalytic activity and tunable active sites.[7,8] The crystal structure of AB_2O_4 consists of rigid sub-lattice of 32 closely packed oxygen anions giving rise to 64 tetrahedral (A)-type and 32 octahedral [B]-type interstitial sites partially occupied by 24 M^{2+} and M^{3+} metal cations. The TM_{oct} plays the dominant role in the catalytic process of OER because the TM_{oct} is preferentially exposed on the near-surface of AB_2O_4 with much shorter distance between TM_{oct}-TM_{oct}, in comparison with other TM oxides, especially perovskite oxides.[9] This means that the OER on the surface of AB_2O_4 will undergo accelerated kinetics due to the synergistic multiple-sites mechanism, rather than the single-site mechanism, unlike perovskites.[10,11] Therefore, developing and designing the octahedral geometry is considered as a paramount strategy to support the commercialization of AB_2O_4 for OER. Beside the advantages like low cost, high abundance, low toxicity, and multiple valence, some spinel oxides even present a prominent Jahn–Teller effect. The valence arrangement of Mn (III) is 3d,[4] which is prone to the John–Teller distortion.[9] In a typical spinel oxide structure, O ions are closely packed, with A^{2+} and B^{3+} ions occupying part of or all the tetrahedral and octahedral sites, respectively. Diverse ion array in the spinel oxides structure has prominent effects on the electronic structure and chemical properties.[2,12] As it is known, heterointerface electrocatalysts typically induce electron transfer occurring at the surface of electrocatalysts.[13–15] Hence, the performance of such

K. B. Ibrahim, T. A. Shifa, E. Moretti, A. Vomiero
Department of Molecular Sciences and Nanosystems
Ca' Foscari University of Venice
Via Torino 155, Venezia Mestre 30170, Italy
E-mail: kassabelay.ibrahim@unive.it; alberto.vomiero@ltu.se
P. Moras
Istituto di Struttura della Materia-CNR (ISM-CNR)
SS 14, Km 163.5, Trieste 34149, Italy
A. Vomiero
Division of Materials Science
Department of Engineering Sciences and Mathematics
Luleå University of Technology
Luleå SE-97187, Sweden

catalysts is greatly dependent on the surface charge state of the designed materials.[16,17]

Thus far, innumerable efforts have been devoted to construct electrocatalysts with a suitable surface electronic structure for enhancing the catalytic activity, like interface engineering to create strong metal support interaction,[18–21] alloying,[22] heteroatom doping,[23] and phase control.[24] Compared with single-component catalysts, heterointerface catalysts have several advantages including the electronic interactions between different components, and the synergistic effects. Apart from this, the general guideline to design active and efficient OER catalysts is to achieve higher intrinsic activity and a high density of interfacial active sites. In this regard, engineering heterointerface is one of the most attractive ways that plays a key role in electrochemical water oxidation.

Inspired by the motivations mentioned above, we designed heterointerfaces between WMn_2O_4 and TiO_2, where WMn_2O_4 nanosheets are uniformly and densely decorated by TiO_2 nanoparticles to maximize the density of the interfacial active sites. WMn_2O_4 exhibits high intrinsic activity, but limited durability and electronic conductivity. TiO_2 nanoparticles can act as a good potential support material for catalysts due to its environmental friendliness, high stability, moderate cost, ability to alter the electronic properties of oxide catalysts, and commercial availability.[3] Thus, the hybridization of WMn_2O_4 with TiO_2 would provide an effective charge transfer, long-term stability, and enhanced adsorption of targeted reactants. In this regard, the resulting heterostructure material would possess a hierarchical structure, which enables a strong electronic coupling and convenient charge transfer at the interconnected interface, thus promoting electron transport. Herein, we introduce a strong metal support interaction (SMSI) effect on WMn_2O_4-TiO_2 heterostructure, hypothesizing that the interface could bring about more active environment to trigger the adsorption and desorption of oxide species to eventually produce O_2 gas via water-splitting. We also demonstrate the change in Mn atomic environment near the metal atoms before the formation of the heterointerface via W atom doping (Scheme S1, Supporting Information); and hence correlate their effect in enhancing the charge transfer phenomena during OER catalysis. The resulting electro-catalyst exhibits an onset overpotential of 200 mV versus reversible hydrogen electrode (RHE), a small Tafel slope (67 mV dec^{-1}), and stable Chronopotentiometric measurement in 0.1 M KOH solution at various current densities (10, 20, and 30 mA cm^{-2}) for a total of 30 h (10 at each current density)

2. Experimental Section

2.1. Synthesis of WMn_2O_4 Nanoflakes and TiO_2 Nanoparticles

In a typical synthesis of WMn_2O_4 nanoflakes, 698 mg of $(Mn(ac))_2$ and 344 mg of WCl_6 were dissolved in 50 mL of deionized (DI) water under gentle magnetic stirring to afford a homogeneous solution. Subsequently, 288 mg of NaOH was dissolved in 5 mL of DI water and added dropwise into the reaction mixture under vigorous stirring. The color of the solution first turned green and gradually evolved into greenish-brown, brown, and finally dark brown with the addition of NaOH. Then, the reaction mixture was transferred into a 100 mL

Teflon-lined stainless steel autoclave and a hydrothermal reaction was carried out at 120 °C for 6 h.[9] The resulting precipitate was collected by centrifugation, was washed thoroughly with anhydrous ethanol and dried in a vacuum at 60 °C for 12 h.

The synthesis procedure for TiO_2 nanoparticles can be found in the Supporting Information.

2.2. Synthesis of WMn_2O_4-TiO_2 Heterostructure

WMn_2O_4-TiO_2 heterostructures were prepared by a modified calcination method. In a typical synthesis, 0.1 g of TiO_2 nanoparticles (1:1 molar ratio of WMn_2O_4 to TiO_2) and WMn_2O_4 nanoflakes were dispersed in 20 mL deionized water. Then, the obtained solution was stirred and heated at a temperature of 80 °C in oil bath. The temperature was slowly increased to 200 °C and kept for 2 h to obtain a complete evaporation and drying of the solvent. Then, the powder was grinded to obtain a uniform size of the heterostructures and then annealed to create strong metal support interaction (SMSI) at 600 °C with a rate of temperature increase equal to 5 °C min^{-1} with 40 sccm an Ar flow with a chamber pressure pumped down to ≈0.1 Pa. The sample was kept at this temperature for 4 h to obtain WMn_2O_4-TiO_2, as schematically represented in **Figure 1**.

2.3. Sample Characterization

The crystalline structure of the samples was investigated through powder X-ray diffraction (XRD). The morphology of the samples was investigated through scanning electron microscopy (SEM) combined with energy dispersive X-ray (EDS) spectroscopy for the elemental analysis. Transition Electron Microscopy (TEM) images were recorded with high-resolution transmission electron microscope. To study the change in electronic environment, X-ray absorption spectroscopy (XAS) and X-ray photoelectron spectroscopy (XPS) measurements were performed with a standard X-ray source and at the VUV-Photoemission beamline of the synchrotron Elettra (Trieste, Italy). Details of the characterization techniques were found in the supporting information.

2.4. Oxygen Generation from Water Splitting

Electrochemical activity measurements were performed using a computer-controlled potentiostat (PGSTAT302N, Metrohm Autolab) assembled with a rotational system (Pine Research Instrumentation, Durham, NC, USA) with a standard three-electrode glass cell (graphite rod as a counter electrode, Ag/AgCl/sat. KCl reference electrode, carbon fiber with catalysts as the working electrode) in 0.1 M KOH electrolyte at room temperature. The working electrode was prepared by ultrasonically dispersing 5 mg of catalysts in 1 mL of isopropanol and DI water (3:1) and Nafion solution (70 μL, 0.05 wt.% in alcohol), and then drop casting the ink on the surface of pretreated carbon fiber. EIS measurements were carried out in 0.1 M KOH electrolyte solution at 25 °C. The detailed procedure is described in the Supporting Information.

**ADVANCED
SCIENCE NEWS**
www.advancedsciencenews.com

NANO · MICRO
small
www.small-journal.com
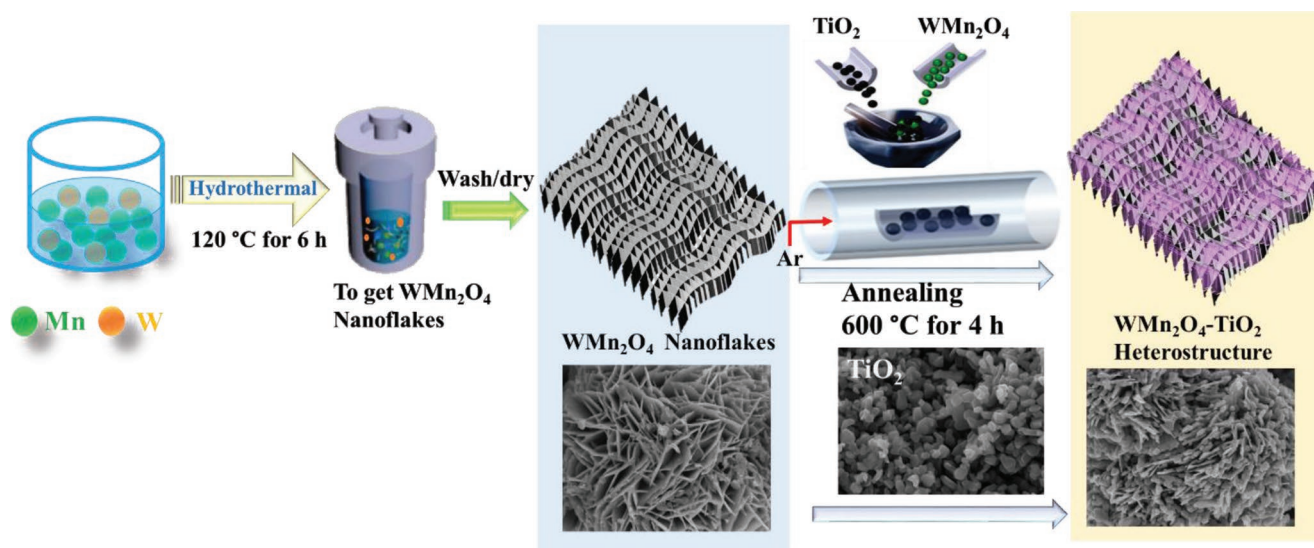
Figure 1. Schematic illustration of WMn_2O_4 nanoflakes via hydrothermal synthesis and synthesis of WMn_2O_4-TiO_2 heterostructure by thermal annealing process.
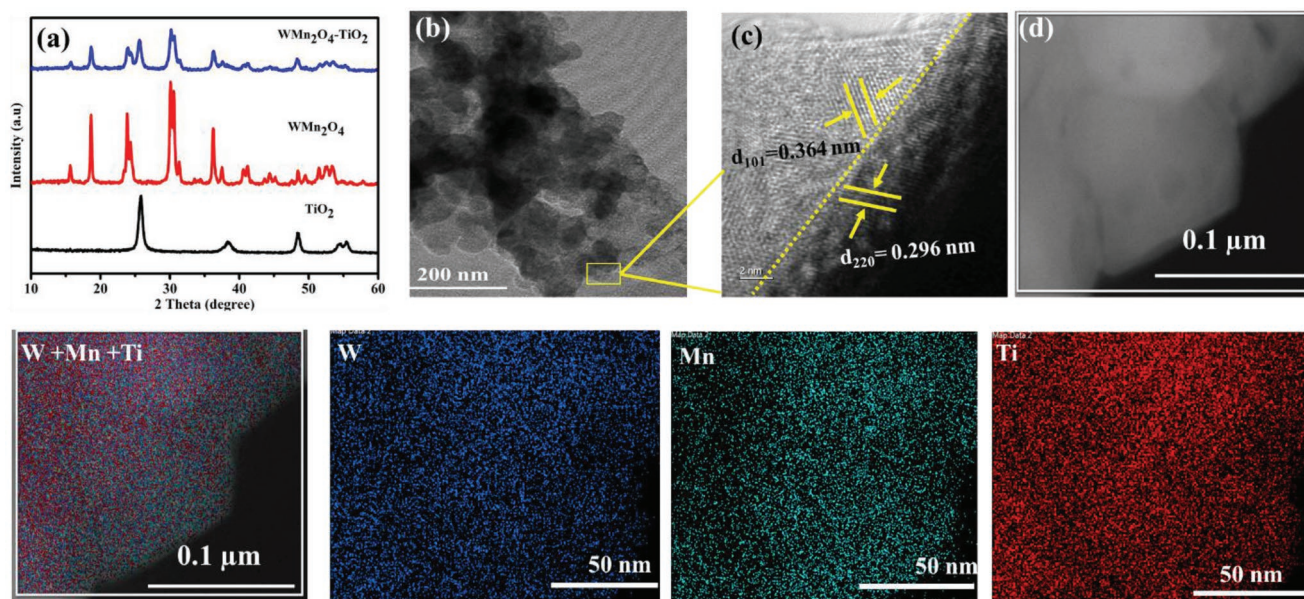
3. Results And Discussion

3.1. Morphological and Structural Characterizations

The scheme for the preparation of the WMn_2O_4-TiO_2 heterostructure is reported in Figure 1. As can be seen in Figure S1a, Supporting Information, a typical SEM image of pristine TiO_2, which possesses well-dispersed nanoparticles. Similarly, Figure S1b, Supporting Information, shows the typical SEM image the WMn_2O_4 nanoflakes. These nanoflakes have a minimum self-aggregation and an open structure, which is advantageous for the electrocatalytic reactions thanks to its high specific surface area and exposed sites. The WMn_2O_4-TiO_2 nanoflakes (Figure S1c, Supporting Information) exhibit an entangled network, in which the TiO_2 nanoparticles are uniformly dispersed on the surface of WMn_2O_4, without agglomeration. Such structure may enhance ion diffusion and electronic motion, and may extend the durability of the electrode. The corresponding EDS elemental mapping (Figure S1d, Supporting Information) reveals the presence of evenly distributed W, Mn, Ti, and O, as expected, with no contaminants, within the detection limit of the technique.

The XRD patterns for the WMn_2O_4 and TiO_2 systems, and the resulting WMn_2O_4-TiO_2 hetero-structure are shown in **Figure 2**a. The typical diffraction peaks from TiO_2 sample (reported for clarity purposes also in Figure S2a, Supporting Information) at 25.38°, 37.90°, 48.14, 54.026° and 55.139 are well assigned to the characteristic reflection of (101), (004), (200), (105) and (211) reflections of an anatase TiO_2 (PDF#89-4921). The reflections from the pristine WMn_2O_4 (reported for clarity purpose also in Figure S2b, Supporting Information) at 15.7°, 18.6°, 23.9°, 30.3°, 36.2°, 37.5°, and 41.2° are attributed to the (111), (220), (311), (222), (400), (440), and (533) lattice planes of a spinel oxide in the interlayer region (PDF #03-0636). After the formation of WMn_2O_4-TiO_2 heterostructure, a superposition of XRD patterns of TiO_2 and WMn_2O_4 is observed, with no appearance of new reflections. This demonstrates the integration of the two materials with high purity and good crystallization, excludes

the formation of new bulk phases. This is clear evidence that the TiO_2 does not diffuse to the lattice of the WMn_2O_4 or does not affect the crystallographic structure of the WMn_2O_4. After the complete synthesis, we can observe numerous TiO_2 nanoparticles decorating the surface of the WMn_2O_4 nanoflakes (Figure S1c, Supporting Information). For further characterization of the heterointerface, TEM and High resolution (HR)-TEM images at a selected area were captured. The corresponding TEM image (Figure 2b) reveals an atomically coupled heterointerface structure with a WMn_2O_4 shell thickness of ≈60 nm. The HR-TEM image (Figure 2c) shows lattice fringes corresponding to the interplanar distance of ≈0.29 and ≈0.36 nm, which can be attributed to the (220) plane of WMn_2O_4 phase and (101) plane of anatase TiO_2, respectively. To further illustrate the coupling interface at the atomic cluster level, we provide extra TEM and HRTEM images in Figure S3a,b, Supporting Information. The two lattice fringes indicate $d_{101} = 0.346$ nm and $d_{220} = 0.296$ nm, corresponding to TiO_2 and WMn_2O_4, respectively. This suggests the coupling interface of TiO_2 and WMn_2O_4 at the atomic cluster level to form heterostructure. The STEM characterization and energy dispersive spectroscopy (EDS) elemental mapping (Figure 2d) shows that W, Mn, and Ti exist in the WMn_2O_4-TiO_2 samples, and that the Ti is uniformly and homogeneously distributed, (see also the EDS imaging from SEM reported in Figure S1d). This result indicates the successful decoration of TiO_2 on WMn_2O_4 flakes, that would deliver a conducive interface for enhanced OER activity. The formation of strong metal support interaction between WMn_2O_4 and TiO_2 is another fascinating phenomenon that probes the electronic effect behind the enhanced catalytic activity.

Given that catalysis is a surface phenomenon, the surface chemical states, and valence state of Mn, W and Ti were assessed by X-ray photoelectron spectroscopy (XPS) in WMn_2O_4, TiO_2, and WMn_2O_4-TiO_2. The Mn 2p3/2 peak (**Figure 3**a) in both WMn_2O_4 and WMn_2O_4-TiO_2 located at 642.4 eV can be associated with contributions of Mn^{3+} oxidation states.[5] The W 4f spectrum in WMn_2O_4-TiO_2 (Figure 3b), presents two

**ADVANCED
SCIENCE NEWS**

www.advancedsciencenews.com

NANO · MICRO

small

www.small-journal.com

Figure 2. a) XRD pattern for TiO_2, WMn_2O_4, and WMn_2O_4-TiO_2. Morphology and elemental distribution of WMn_2O_4-TiO_2 heterostructure. b) TEM and c) HRTEM image of WMn_2O_4-TiO_2. d) STEM image and elemental maps showing the uniform distribution of W, Mn, and Ti. The bottom line collects EDS mapping related to (d) of W, Mn, Ti elements, and their overlapped map (right side).
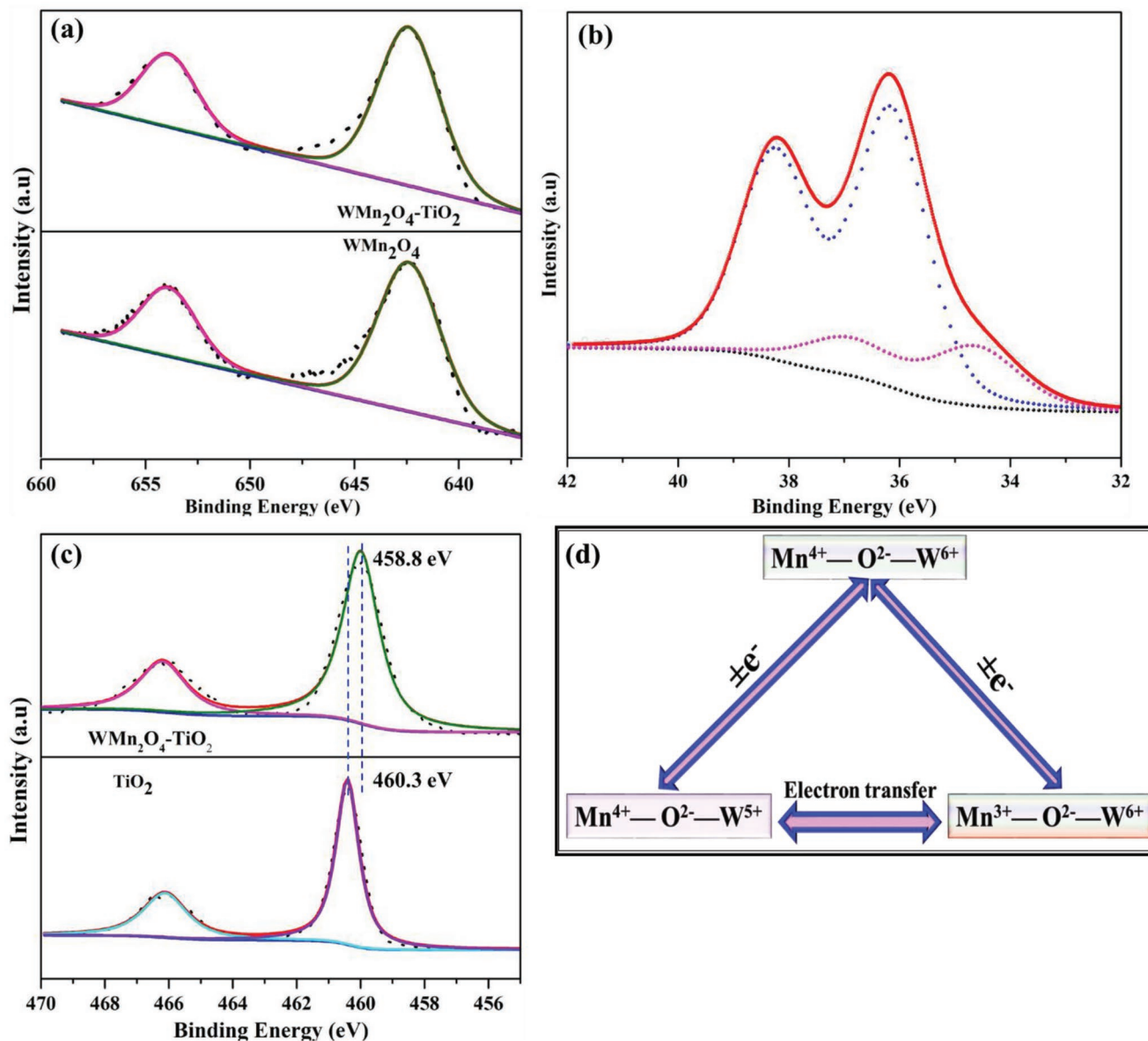
doubles corresponding to the two different oxidation states of W. The doublet with the W 4f7/2 peaks at 36.18 eV corresponds to W^{+6}[25] and the doublet with the W 4f7/2 peak at 34.58 eV to W^{+5}.[26] The doublet with the W 4f7/2 peaks corresponding to W^{+6} and, W^{+5} for the pristine WMn_2O_4 (Figure S4a, Supporting Information) also appeared in the respective binding energy. However, the low penetration depth profile of XPS spectra limit to see the change in electronic structure on W 4f and Mn 2p spectra in WMn_2O_4 and WMn_2O_4-TiO_2 samples. Therefore, we use XAS characterization for best penetration depth profile and sensitive toward even smaller changes in electronic structures.

The Ti 2p3/2 spectra in WMn_2O_4-TiO_2 (Figure 3c) centered at 458.8 shift to lower BE compared to the Ti 2p3/2 spectra centered at 460.3 eV in TiO_2. This negative shift in Ti 2p spectra in the heterostructure catalysts is due to the decrease in oxidation number during thermal annealing to different oxidation states of Ti. During thermal annealing, TiO_2 commonly reduces to different Magnéli phase oxides as described with the general formula $Ti_nO_{2n-1}, 3 < n < 10$.[20,27] In the WMn_2O_4 sample, the O1s XPS spectrum (Figure S4b, Supporting Information) shows three deconvoluted peaks at binding energies of 529.7 eV and 531.2 eV, assigned to lattice oxygen, and at 533.02 eV, assigned to surface defects and/or adsorbed surface hydroxyls. The lattice oxygen peaks can be associated to the nature of oxides as in $Mn(OH)_2$ (529.7 eV) and MnO_2 (531.2 eV). Generally, the change in the oxidation state in the redox couples of Mn^{3+} and W^{5+}/W^{6+} (i.e., $W^{6+} + Mn^{3+} \leftrightarrow W^{5+} + Mn^{4+}$) is induced during annealing to construct surface heterointerface material that improves the electron transfer (Figure 3d).

To gather further information on the different crystal structures in the samples and on the role of each element, we applied X-ray absorption near edge fine structure (XANES) spectroscopy. Metal K-edges absorption spectra are very sensitive to the interactions with the neighboring atoms and the chemical

states of the atoms for the 3d transition metals. The K-edge for an absorption process is due to 1s electrons transition to the empty levels (3d, 4p) over the Fermi level as a final state. Actually, the 1s → 3d transition is forbidden due to a combination of a strong 3d–4p mixing and the overlap of metal 3d orbitals with 2p orbitals of surrounding O atoms.[28] The 3d levels are located just below the Fermi level and can give information about the binding properties of the source atoms. The pre-edge structure may occur just below the main absorption edge and gives information about the forbidden transitions and crystal disorder. On the other side, the post-edge part lies just beyond the main edge and provides information about the interactions with the closest neighboring atoms. The white line part is the large, prominent peak just above the edge. Particularly in L or M edge spectra, it provides information about the d-orbital occupancy.[29]

As a result, the Mn K edge spectra were taken before and after OER to see how the change in the Mn valence state is affected. As a result, the pre-edge feature ≈6540.6 eV in the Mn K-edge spectra in both WMn_2O_4, and WMn_2O_4-TiO_2 is due to quadrupole 1s-3d and/or modifications of the dipole transition probability due to the hybridization between 3d and 4p states.[30] In Mn K pre-edge spectra, No shift was observed in the position, but the intensity of this feature decreased in WMn_2O_4-TiO_2 compared to pristine WMn_2O_4 (**Figure 4**a inset). This is due to the high degree of disorder in the Mn environment during the surface annealing to form the heterointerface. Nevertheless, this change is pronounced even after OER in the WMn_2O_4-TiO_2, indicating the oxidation state of Mn keeps changing. The energy of the main edge shows a positive shift in WMn_2O_4-TiO_2 compared to WMn_2O_4 (Figure 4a) ascribed to the higher oxidation state of Mn and change of the electronic structure around the Mn atoms, as a result of the heterointerface formation. This is also in agreement with the XPS results.

**ADVANCED
SCIENCE NEWS**

www.advancedsciencenews.com

NANO · MICRO

small

www.small-journal.com

Figure 3. XPS spectra of a) Mn 2p, b) W 4f in WMn_2O_4-TiO_2, c) Ti 2p in TiO_2 and WMn_2O_4-TiO_2. d) The electron transfers of redox couples of Mn^{3+}/Mn^{4+} and W^{6+}/W^{5+}.

Similarly, the local structure and the valence state of the W species are determined by the position of the W edge. In this case, the local symmetry is determined by the area of the pre-edge peak of the W L-edge XANES, which is due to a 2s-5d transition. The 2s-5d transition is a dipole-forbidden transition for regular octahedral symmetry; however, this is partially allowed for a distorted octahedral structure, which gives rise to the absence of an inversion symmetry because the p orbitals are mixed with 5d orbitals. Therefore, a W unit with tetrahedral symmetry exhibits a large pre-edge peak area in W L-edge XANES. Figure 4b depicts the normalized XANES spectra of the WMn_2O_4-TiO_2 and reference samples. In WMn_2O_4-TiO_2 sample, the energy of the absorption edge at 10.2 keV implies a valence state of W^{5+}. Compared to W foil and WMn_2O_4, the W L-edge in WMn_2O_4-TiO_2 shows a positive shift that confirms the

oxidation of W^{5+}. This result is consistent with our XPS results. The intensity of the white line increases in the WMn_2O_4-TiO_2 sample, compared to WMn_2O_4, suggests a lower octahedral symmetry around W atoms and increase in the disorder of the W–O bond.

It is worth noting that the pre-edge regime of the Ti K-edge is very sensitive to the local structure geometry and coordination environment. The pre-edge feature of Ti K-edge XANES originates from the 1s–3d transition and appears due to the polarization of p-orbitals and strong 3d–4p orbital mixing.[31] As a result, the pre-edge of Ti k-edge shows three different peaks represented as feature A_1, A_2, and A_3. A_1 is related to the Ti 1s-3d (t2g) quadrupole transition and varies upon structural changes in the first coordination shell of Ti.[32,33] Thus, the Ti K-edge in the hetero-structured sample (WMn_2O_4-TiO_2)
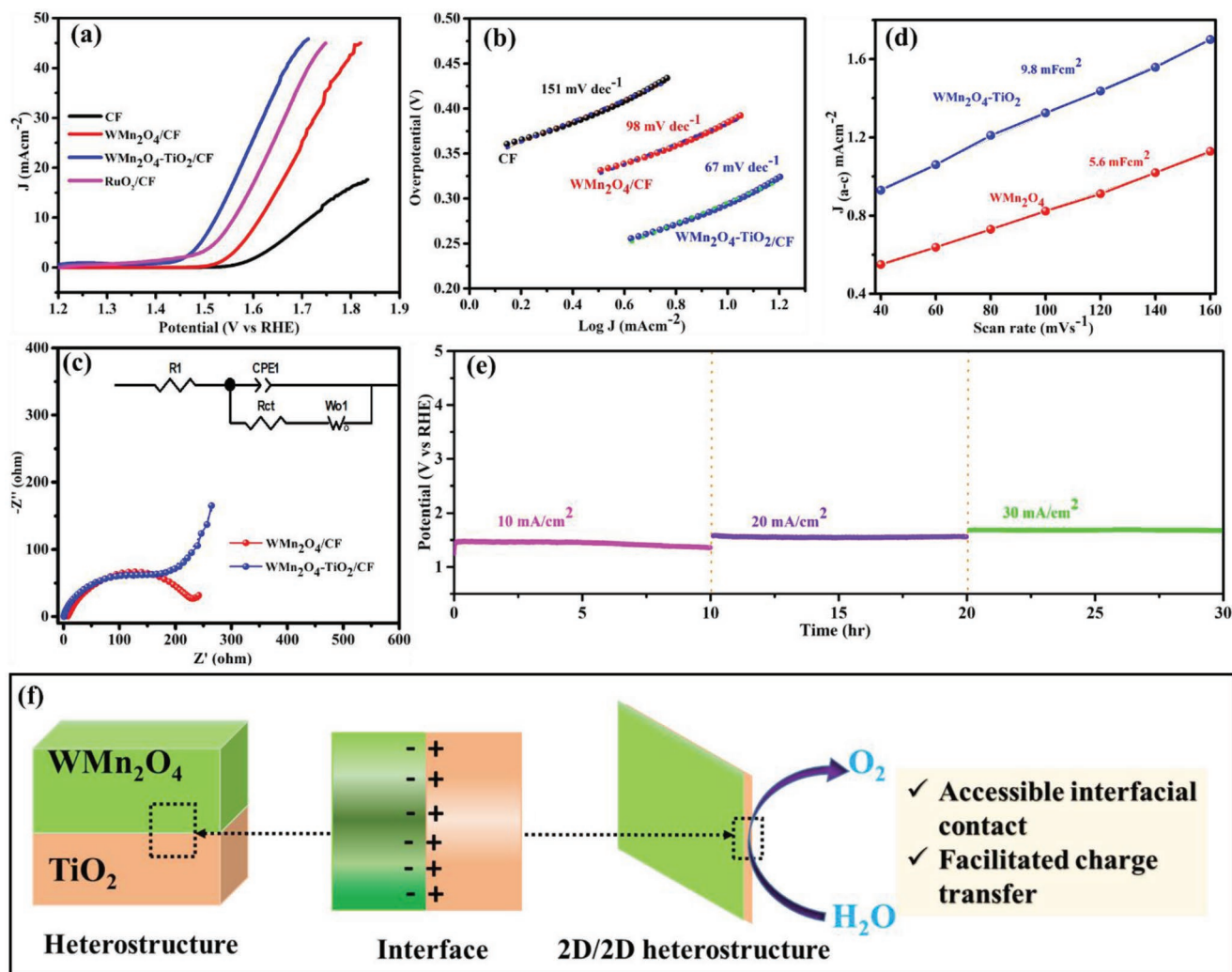
2204765 (5 of 10)
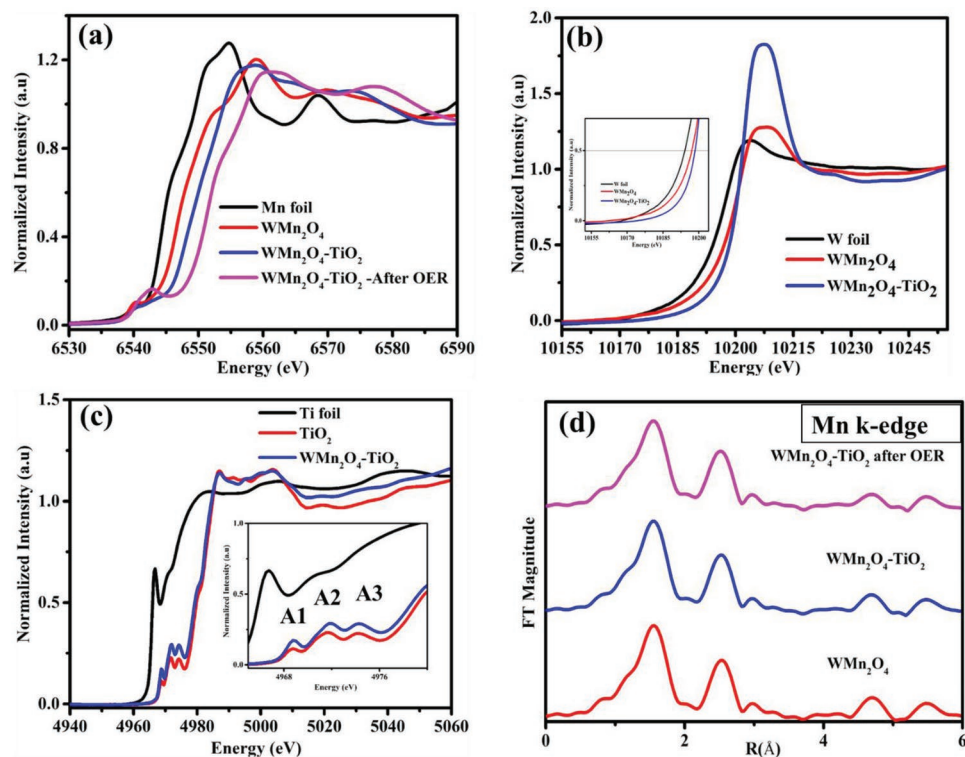
Figure 4. Structure analysis of WMn_2O_4-TiO_2 by X-ray absorption fine structure (XAFS). X-ray absorption near edge spectra (XANES) a) Mn K-edge b) W L-edge and c) Ti K-edge. d) Mn K-edge EXAFS spectra

displays the increased intensity of the pre-edge peak with a decrease in coordination number as compared to TiO_2, (Figure 4c) associated with severe Ti site distortions. The absorption edge shifts towards lower energy for WMn_2O_4-TiO_2 in comparison with the TiO_2 sample, probably due to the reduction of TiO_2 to different Magnéli phase oxides as described with the general formula Ti_nO_{2n-1}, $3 < n < 10$ during thermal annealing for the heterostructure formation.[20,27] Furthermore, to study the local structure and coordination environment, Fourier transforms (FTs) of the EXAFS data for WMn_2O_4, WMn_2O_4-TiO_2, and WMn_2O_4-TiO_2 after OER is analyzed. As shown in Figure 4d, the peak at 1.76 Å in radial distribution function of the Mn K-edge is assigned to Mn–O coordination, and the peaks at ≈3.00 Å are associated with Mn–M (M = Mn, W, Ti) coordination peaks. As can be seen in Figure 4d the decreased intensity of these coordination spheres in WMn_2O_4-TiO_2 relative to WMn_2O_4 evidences a decrease in the average coordination number (*N*) of Mn–O and Mn–M shells in WMn_2O_4-TiO_2. This could be related to the induced vacancies around the metal and oxygen, that are acknowledged to boost catalysis in various applications. Meantime, the edge position in WMn_2O_4-TiO_2 shows a small shift relative to WMn_2O_4, indicating the structural distortion due to heterointerface.

3.2. OER Performance of $WMnO_4$-TiO_2 Heterointerface

To understand how the interface affects the OER catalytic performance, the prepared materials were directly evaluated in 0.1 M KOH solution. The electro-catalytic activity of the catalysts supported on carbon fiber was characterized by linear sweep voltammetry (LSV) in O_2 and Ar saturated 0.1 M aqueous KOH solutions (**Figure 5**), employed to assess the OER kinetics of the catalysts. As can be seen in Figure 5a,b, the heterostructure, benefitting from the active interface, generates a current of 10, 20, and 30 mA cm^{-2} under an applied potential of 1.5 V, 1.55 V, and 1.6 V versus RHE, respectively, with a significant improvement compared to WMn_2O_4 (10 mA cm^{-2} @ 1.6 V, 20 mA cm^{-2} @1.65 V and 30 mA cm^{-2} @1.7 V) and RuO_2 (10 mA cm^{-2} @ 1.56 V, 20 mA cm^{-2} @ 1.62 V and 30 mA cm^{-2} @1.67 V). In fact, in the heterointerface catalyst, the electrons can be transferred from one component to another through the boundary surface, that modulates the current density around the active sites. The changes in chemical composition or crystal structure due to strong metal support interaction (SMSI), the setting of atoms at the interface are different from the bulk material, which can induce electronic and geometric effect and new chemical bonding at the boundary surface.[34] To confirm that the interface construction is beneficial to increase the intrinsic activity of the materials, we report the ECSA normalized LSV for WMn_2O_4 and WMn_2O_4-TiO_2 in Figure S5a, Supporting Information. As a result, the intrinsic activity for WMn_2O_4-TiO_2 shows an increase after normalization by ECSA, compared to WMn_2O_4, thus confirming that the interface construction is beneficial to increase the intrinsic activity. The increased current in WMn_2O_4 after ECSA normalization might be actually due to thermal annealing affects the surface area for WMn_2O_4-TiO_2. To remove the ambiguity on the origin of the enhanced activity (resulting from thermal annealing or from the

**ADVANCED
SCIENCE NEWS**

www.advancedsciencenews.com

**NANO · MICRO
small**

www.small-journal.com

Figure 5. Electrocatalytic water oxidation performance. a) LSV curves, scan rate: 5 mV s^{-1}. b) Tafel plots extracted from LSV curves. c) Double-layer capacitance (C_{dl}) measurements of WMn_2O_4-TiO_2 and WMn_2O_4. d) Comparison of Nyquist plots for the WMn_2O_4-TiO_2 versus WMn_2O_4 samples. e) Chronopotentiometric run of WMn_2O_4-TiO_2 for the long term durability test at 10, 20, and 30 mA cm^{-2}. f) Schematic structures of bulk heterointerface and 2D/2D heterointerface with a coupled interface.

introduction of the heterostructure), we tested the OER activity of WMn_2O_4 after thermal annealing as can be seen in Figure S5b, Supporting Information. The thermally synthesized WMn_2O_4 shows worsened OER activity (1.6 V, onset potential) compared to the WMn_2O_4 sample synthesized via the hydrothermal route. Thus, we can assure that the enhanced OER activity is resulting from the introduction of TiO_2 to form heterostructure. As listed in Table S1, Supporting Information, the optimized WMn_2O_4-TiO_2 heterostructure is one of the best among the most active recently reported oxide OER catalysts.

To further understand the kinetics of the OER, Tafel slope were extracted from the polarization curves. The WMn_2O_4-TiO_2 hetero-structure exhibited Tafel slope of 67 mV dec^{-1}, much lower than the WMn_2O_4 (98 mV dec^{-1}) (Figure 5b). The lower Tafel slope suggests the fast reaction kinetics for oxygen evolution and rapid electron transfer in the heterointerface. The significant difference in intrinsic reaction kinetics between WMn_2O_4-TiO_2 and WMn_2O_4 samples also contributes to the

different catalytic performance. The formation of heterostructure is associated with the abundant exposure of active sites as a result of the new interface formation between dissimilar materials. Therefore, it is crucial to understand the electrochemical active area of catalysts for OER, which can be estimated by the double layer capacitance (C_{dl}) around the electrode surface. To unveil this, we calculated the C_{dl} by monitoring the current density in the non-Faradic region with different scan rates. The CVs runs for obtaining these data are presented in Figure S5c,d, Supporting Information. Figure 5c depicts a higher value of C_{dl} in the case of WMn_2O_4-TiO_2 (9.8 mF cm^{-2}) than WMn_2O_4 (5.6 mF cm^{-2}). The large electrochemical double-layer capacitance indicates the increased density of exposed active sites, which is one of the possible reasons for the enhanced OER activity. To confirm the high catalytic activity of the heterostructured material, electrochemical impedance spectroscopies (EIS) is analyzed in the frequency range from 100 kHz to 0.01 Hz as depicted in Figure 5c. The Nyquist plots

were fitted by using a simple Randles equivalent circuit model, consisting of solution resistance (R_s), and charge transfer resistance (R_{ct}) that is concerned with OER kinetics, that are related to reaction rate. As can be seen in Figure 5c and Table S2, Supporting Information, WMn$_2$O$_4$-TiO$_2$ displayed the R_{ct} (130 Ω), which is lower than that of WMn$_2$O$_4$ (205 Ω) suggesting facile electrode kinetics and faster electronic transport. This highlights that the formation of a heterointerface between TiO$_2$ and WMn$_2$O$_4$ triggers efficient electron transfer that increase electronic conductivity, thereby yielding accelerated O$_2$ gas evolution.

To evaluate electrochemical stability, long-term test was conducted using chronopotentiometric measurement at various current densities (10, 20, and 30 mA cm^{-2}) for a total of 30 h (10 at each current density). As represented in Figure 5d, WMn$_2$O$_4$-TiO$_2$ heterostructure demonstrates very good stability with only minor degradation over long-term testing. It retains 99.8%, 99.6%, and 99.2% activity at 10, 20, and 30 mA cm^{-2}, respectively. As depicted in Figure 5f, the presence of TiO$_2$ in the WMn$_2$O$_4$ composite also enables a stronger electronic coupling with the electrocatalyst itself and allows faster charge transfer and increase accessible interfacial contact that accelerate OER. We conclude that the trapped Mn^{3+} states are essential for the formation of structurally highly flexible local clusters that could resemble the active sites for water oxidation catalysis. Additionally, we would like to stress that this study again indicates that the stabilization of a fraction of Mn^{3+}centers at water oxidation potentials via W and Ti seems to be decisive for catalytic activity.

To get ultrafast OER performance the energy loss between electrodes and active sites, the electronic conductivity, and the interface between catalyst-catalyst support and catalyst-electrolyte are minimized. In order to achieve this, heterostructure catalyst with strong metal support interaction (SMSI) in which one can compensate the drawback of the other as schematically represented in **Figure 6** needs to be designed and developed in the field of water splitting catalyst. Furthermore, the heterostructure also exposes more assessable active sites via catalyst surface reconstruction with improved reaction kinetics, giving consequently superior activity. Generally, designing heterointerface 2D material accelerates charge transfer at the electrode/electrolyte interface and decreases the overall charge transfer resistance by enhancing the electronic conductivity, that induces the improvement of the OER performance.

To examine the structural stability of WMn$_2$O$_4$-TiO$_2$ catalyst, post-OER characterization of the catalyst was performed by XRD, and XPS. Interestingly, in the post-OER XRD measurement depicted in **Figure 7**a (top panel), no observable new phases or peak shift are recorded, which further demonstrates the good structural stability of the as-synthesized catalyst. The broad peak ≈2Θ = 25 results from the carbon fiber used as a substrate for OER measurement. Figure 7b-d shows the XPS results of Mn 2p, W4f, and Ti 2p for the WMn$_2$O$_4$-TiO$_2$ electrode after the OER. Manganese shows two components. The Mn 2p3/2 peak centered at a BE value of 642.4 eV shows a slight positive shift (0.9 eV) compared to the system before OER. the Minor Mn2p3/2 peak centered at BE of 644.6 eV is associated to an oxidation state between 3 and 4. In the W4f spectra, we observe two doublets attributed to W^{5+} (blue line) and W^{6+} (pink line). The shoulder peak located ≈34 eV corresponds to K3s (from the electrolyte, 0.1 M KOH) at the sample surface. The Ti doublet with Ti 2p3/2 centered at 459.8 eV corresponds to Ti^{4+}. A smaller component with the Ti2p3/2 peak centered 458.6 eV is ascribed to Ti^{3+} (defect) in WMn$_2$O$_4$-TiO$_2$ or Ti^{3+} in Ti$_2$O$_3$.[35] Therefore, we identify the W, Mn, and Ti elements with different oxidation state in the expected binding energy ranges. The existence of viable oxidation states of W, Mn, and Ti benefit for enhanced OER activity.

4. Conclusion

In conclusion, we have demonstrated cost-effective and ultrafast OER active catalyst via heterointerface engineering. Interface engineering to form SMSI has been recently recognized
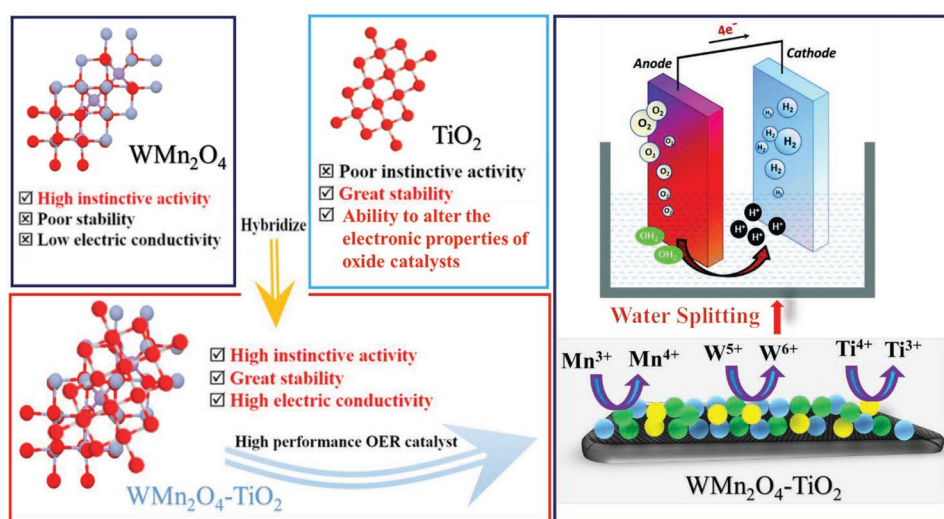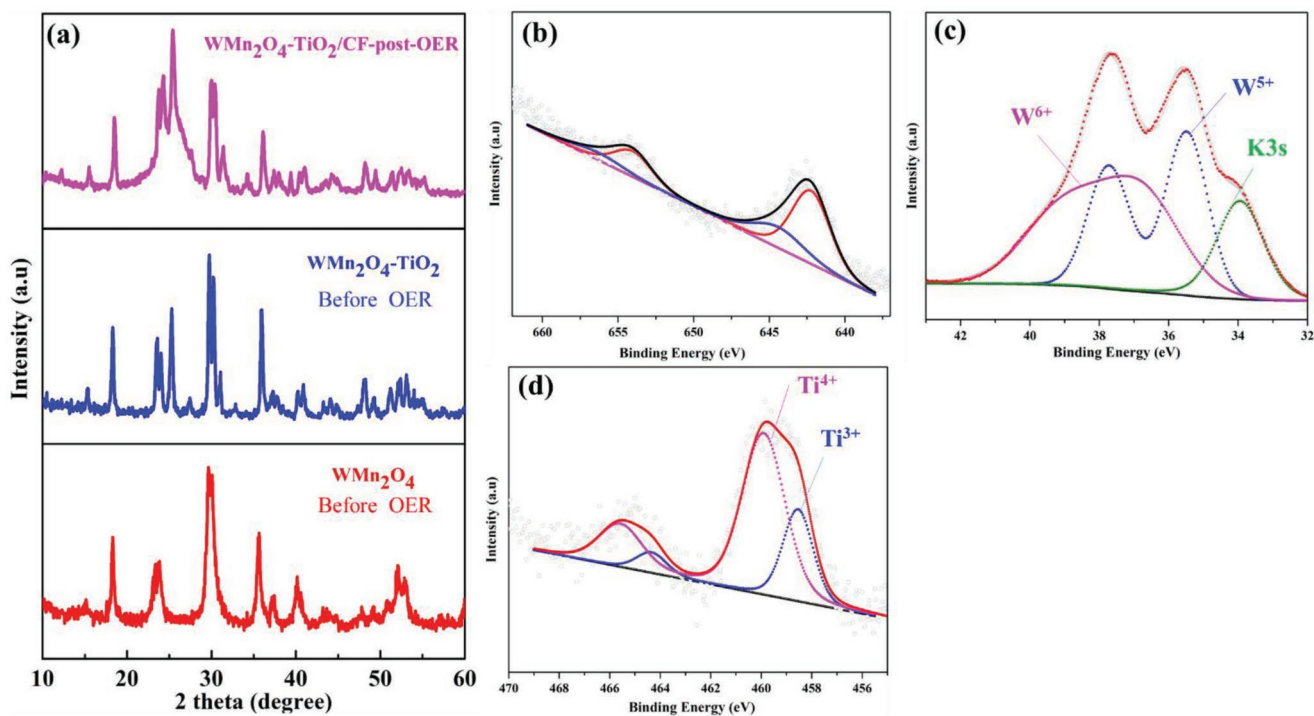

Figure 6. Schematic illustration for the modified hetero-structure materials and its application in water splitting.

Figure 7. a) XRD data for WMn$_2$O$_4$ before OER (red line), WMn$_2$O$_4$-TiO$_2$ before OER (blue line), and WMn$_2$O$_4$-TiO$_2$ post OER (pink line) and post OER XPS spectra of b) Mn 2p c) W 4f and d) Ti 2p in WMn$_2$O$_4$-TiO$_2$.

as one of the most promising strategies to develop efficient water oxidation electrocatalysts. This heterointerface gave rise to the exposure of the active site, which significantly accelerates the OER performance. In the heterointerface catalysts, electrons can be rearranged on heterostructures to modify the exposure of active sites and accelerate the reaction kinetic. As a result, the heterostructure benefitting from the active interface exhibits potent OER catalytic performance with lower overpotential (200 V), with an improvement of 70 mV as compared to a single-component analog of WMn$_2$O$_4$ (270 V). This overpotential shows only negligible change within 30 h of test, suggesting the heterointerface increases the exposure of active species and prevents the collapse of the spinel oxide. Furthermore, the enhanced activity and long-term durability is believed to be originated from the synergetic effect between WMn$_2$O$_4$ and TiO$_2$, leading to higher charge carrier density, and enhanced conductivity. To confirm different surface-interface and electronic properties, XAS, and HR-TEM characterization tools were used, enabling a full description of the heterointerface from the structural as well as functional point of view. Finally, our approach reveals a novel strategy to manipulate the surface/interface charge states of electrocatalysts for accelerated oxygen evolution, representing a significant advancement in the field of H$_2$ production through the overall water-splitting process.

Supporting Information

Supporting Information is available from the Wiley Online Library or from the author.

Conflict of Interest

The authors declare no conflict of interest.

Data Availability Statement

The data that support the findings of this study are available from the corresponding author upon reasonable request.

ADVANCED
SCIENCE NEWS

www.advancedsciencenews.com

NANO · MICRO
small
www.small-journal.com

[1] X. Li, X. Hao, A. Abudula, G. Guan, *J. Mater. Chem. A* **2016**, *4*, 11973.

[2] H.-F. Wang, C. Tang, B.-Q. Li, Q. Zhang, *Inorg. Chem. Front.* **2018**, *5*, 521.

[3] K. B. Ibrahim, M.-C. Tsai, S. A. Chala, M. K. Berihun, A. W. Kahsay, T. A. Berhe, W.-N. Su, B.-J. Hwang, *J Chin Chem Soc* **2019**, *66*, 829.

[4] Y. Zhou, H. Liu, X. Gu, X. Wu, L. Feng, *Carbon Energy* **2022**, 1.

[5] M. Khan, E. Suljoti, A. Singh, S. A. Bonke, T. Brandenburg, K. Atak, R. Golnak, L. Spiccia, E. F. Aziz, *J. Mater. Chem. A* **2014**, *2*, 18199.

[6] W. H. Bragg, *Nature* **1915**, *95*, 561.

[7] A. K. Kushwaha, Ş. Uğur, S. Akbudak, G. Uğur, *J. Alloys Compd.* **2017**, *704*, 101.

[8] Y. Liang, Y. Li, H. Wang, J. Zhou, J. Wang, T. Regier, H. Dai, *Nat. Mater.* **2011**, *10*, 780.

[9] P. W. Menezes, A. Indra, N. R. Sahraie, A. Bergmann, P. Strasser, M. Driess, *ChemSusChem* **2015**, *8*, 164.

[10] W. Wang, L. Kuai, W. Cao, M. Huttula, S. Ollikkala, T. Ahopelto, A.-P. Honkanen, S. Huotari, M. Yu, B. Geng, *Angew. Chem., Int. Ed.* **2017**, *56*, 14977.

[11] T. Zhao, S. Gadipelli, G. He, M. J. Ward, D. Do, P. Zhang, Z. Guo, *ChemSusChem* **2018**, *11*, 1295.

[12] K. B. Ibrahim, W. N. Su, M. C. Tsai, A. W. Kahsay, S. A. Chala, M. K. Birhanu, J. F. Lee, B. J. Hwang, *Mater. Today Chem.* **2022**, *24*, 100824.

[13] Z. Li, M. Hu, P. Wang, J. Liu, J. Yao, C. Li, *Coord. Chem. Rev.* **2021**, *439*, 213953.

[14] L. Xu, S. Wu, X. He, H. Wang, D. Deng, J. Wu, H. Li, *Chem. Eng. J.* **2022**, *437*, 135291.

[15] K. Wang, Z. Wang, Y. Liu, J. Liu, Z. Cui, X. Zhang, F. Ciucci, Z. Tang, *Chem. Eng. J.* **2022**, *427*, 131966.

[16] S. Ni, H. Qu, Z. Xu, X. Zhu, H. Xing, L. Wang, J. Yu, H. Liu, C. Chen, L. Yang, *Appl. Catal., B* **2021**, *299*, 120638.

[17] S. Chandrasekaran, N. Li, Y. Zhuang, L. Sui, Z. Xiao, D. Fan, V. Aravindan, C. Bowen, H. Lu, Y. Liu, *Chem. Eng. J.* **2022**, *431*, 134073.

[18] B. Wang, K. Srinivas, X. Wang, Z. Su, B. Yu, X. zhang, Y. Liu, F. Ma, D. Yang, Y. Chen, *Nanoscale* **2021**, *13*, 9651.

[19] W. Li, Y. Niu, X. Wu, F. Wu, T. Li, W. Hu, *ACS Sustainable Chem. Eng.* **2020**, *8*, 4658.

[20] K. B. Ibrahim, W.-N. Su, M.-C. Tsai, S. A. Chala, A. W. Kahsay, M.-H. Yeh, H.-M. Chen, A. D. Duma, H. Dai, B.-J. Hwang, *Nano Energy* **2018**, *47*, 309.

[21] J. Chen, C. Fan, X. Hu, C. Wang, Z. Huang, G. Fu, J.-M. Lee, Y. Tang, *Small* **2019**, *15*, 1901518.

[22] Z. Li, X. Wu, X. Jiang, B. Shen, Z. Teng, D. Sun, G. Fu, Y. Tang, *Adv. Powder Mater.* **2022**, *1*, 100020.

[23] Y. Zuo, D. Rao, S. Ma, T. Li, Y. H. Tsang, S. Kment, Y. Chai, *ACS Nano* **2019**, *13*, 11469.

[24] J. Zhou, L. Yuan, J. Wang, L. Song, Y. You, R. Zhou, J. Zhang, J. Xu, *J. Mater. Chem. A* **2020**, *8*, 8113.

[25] B. Weng, J. Wu, N. Zhang, Y.-J. Xu, *Langmuir* **2014**, *30*, 5574.

[26] M. Riley, W. Vermerris, *Nanomaterials* **2017**, *7*, 94.

[27] C. Yao, F. Li, X. Li, D. Xia, *J. Mater. Chem.* **2012**, *22*, 16560.

[28] H.-L. Yu, K. B. Ibrahim, P.-W. Chi, Y.-H. Su, W.-T. Chen, S.-C. Tseng, M.-T. Tang, C.-L. Chen, H.-Y. Tang, C.-W. Pao, K.-H. Chen, M.-K. Wu, H.-L. Wu, *Adv. Funct. Mater.* **2022**, *32*, 2112394.

[29] S. A. Chala, M.-C. Tsai, W.-N. Su, K. B. Ibrahim, A. D. Duma, M.-H. Yeh, C.-Y. Wen, C.-H. Yu, T.-S. Chan, H. Dai, B.-J. Hwang, *ACS Catal.* **2019**, *9*, 117.

[30] S. A. Chala, M.-C. Tsai, W.-N. Su, K. B. Ibrahim, B. Thirumalraj, T.-S. Chan, J.-F. Lee, H. Dai, B.-J. Hwang, *ACS Nano* **2020**, *14*, 1770.

[31] A. Zabilska, A. H. Clark, B. M. Moskowitz, I. E. Wachs, Y. Kakiuchi, C. Copéret, M. Nachtegaal, O. Kröcher, O. V. Safonova, *JACS Au* **2022**, *2*, 762.

[32] M. Arshad, W. Khan, P. Rajput, M. Kumar, M. Abushad, S. Husain, *Ceram. Int.* **2022**, *48*, 14156.

[33] G. S. Henderson, F. M. F. d. Groot, B. J. A. Moulton, in *Spectroscopic Methods in Mineralogy and Material Sciences*, (Eds.: H. Grant, N. Daniel, D. Robert, D. Gruyter), De Gruyter, Germany **2014**, pp. 75–138.

[34] D. G. Wickham, W. J. Croft, *J. Phys. Chem. Solids* **1958**, *7*, 351.

[35] Y. Li, Y. Weng, J. Zhang, J. Ding, Y. Zhu, Q. Wang, Y. Yang, Y. Cheng, Q. Zhang, P. Li, J. Lin, W. Chen, Y. Han, X. Zhang, L. Chen, X. Chen, J. Chen, S. Dong, X. Chen, T. Wu, *NPG Asia Mater.* **2018**, *10*, 522.